

MIT Open Access Articles

*Satellite Retrievals of Arctic and Equatorial Rain
and Snowfall Rates Using Millimeter Wavelengths*

The MIT Faculty has made this article openly available. **Please share**
how this access benefits you. Your story matters.

Citation: Surussavadee, C., and D.H. Staelin. "Satellite Retrievals of Arctic and Equatorial Rain and Snowfall Rates Using Millimeter Wavelengths." IEEE Transactions on Geoscience and Remote Sensing 47.11 (2009): 3697–3707. © Copyright 2009 IEEE

As Published: <http://dx.doi.org/10.1109/tgrs.2009.2029093>

Publisher: Institute of Electrical and Electronics Engineers

Persistent URL: <http://hdl.handle.net/1721.1/74521>

Version: Final published version: final published article, as it appeared in a journal, conference proceedings, or other formally published context

Terms of Use: Article is made available in accordance with the publisher's policy and may be subject to US copyright law. Please refer to the publisher's site for terms of use.



Satellite Retrievals of Arctic and Equatorial Rain and Snowfall Rates Using Millimeter Wavelengths

Chinnawat Surussavadee, *Member, IEEE*, and David H. Staelin, *Life Fellow, IEEE*

Abstract—A new global precipitation retrieval algorithm for the millimeter-wave Advanced Microwave Sounding Unit is presented that also retrieves Arctic precipitation rates over surface snow and ice. This algorithm improves upon its predecessor by excluding some surface-sensitive channels and by reducing the number of principal components (PCs) used to represent those that remain. The training sets were also modified to better represent cold regions. The algorithm still incorporates conversion of brightness temperatures to nadir, spatial filtering to better detect pixels scattering near 54 GHz, PC filtering of surface effects, and use of separate neural networks trained with the fifth-generation National Center for Atmospheric Research/Penn State Mesoscale Model (MM5) for land and sea, where warm and cold ocean are now treated differently. The validity of the snowfall detections is supported by nearly coincident CloudSat radar observations, and the physics of the model is largely validated by the reasonable agreement in annual precipitation obtained for 231 globally distributed rain gauges, including many at latitudes where snowfall dominates. Observed annual global precipitation statistics are also presented to permit comparisons with other algorithms and sensors.

Index Terms—Advanced Microwave Sounding Unit (AMSU), Arctic, microwave precipitation estimation, precipitation, remote sensing, satellite, snow.

I. INTRODUCTION

DEVELOPMENT of retrieval algorithms typically begins with simple versions that are extensively tested against truth to expose weaknesses addressed in the next iteration. This paper describes our fifth such iteration for millimeter-wavelength precipitation retrievals 23–191 GHz [1]–[4]. It better integrates the two current physical approaches based on scattering and on absorption/emission against a contrasting thermal background and, for the first time, it retrieves Arctic precipitation over the polar ice cap. Comparison with other algorithms and sensors suggests challenges and approaches for future iterations.

The first papers employing scattering [5] to detect precipitation used the opaque 54-GHz oxygen band to avoid surface

effects. These detections were based on cold spots identified spatially instead of by their absolute values. This approach was later extended to the opaque 183-GHz water-vapor channels, which had two advantages: The spatial resolution was higher (~ 15 km), and spatial filtering was not required because absolute 183-GHz brightness temperatures below a frequency-dependent threshold can be reached only by scattering [2]. Moreover, different 183-GHz channels sense scattering at different altitudes, thereby yielding additional information about convective intensity. Scattering in window channels, particularly near 89 GHz, has also been used to detect precipitation over warm backgrounds, but such channels over precipitation-free ocean and small bodies of water can register comparably low brightness temperatures, producing retrieval ambiguities requiring resolution [6].

Advanced Microwave Sounding Unit (AMSU) radiances are linked to surface precipitation rates because average precipitation rates are related to vertical wind times absolute humidity, both of which AMSU indirectly senses, i.e., water vapor rising rapidly (in millimeters per hour) toward lower temperatures will eventually precipitate. Vertical wind can be inferred from: 1) cell-top altitudes retrieved using “altitude slicing” in both the 53- and 183-GHz bands (different channels penetrate to different altitudes); 2) altitude profiles of hydrometeor size distributions revealed by differences in scattering cross sections sensed near 53 and 183 GHz (large hydrometeors require high winds); and 3) cell-top albedos. By combining the 53-GHz band temperature profile information with the 183-GHz humidity information, the absolute humidity profile can also be estimated. Finally, the 23.8-, 31.4-, and 50.2-GHz window channels reveal the opacity of oceanic precipitation seen in emission. These radiometric signatures from hydrometeors aloft can be misleading if the precipitation evaporates near the surface; our recent results suggest such evaporation is a prime source of overestimation over desert-like terrain [7].

Retrieval errors will be introduced unless the training process faithfully predicts AMSU radiances. This fidelity was tested by comparing histograms of observed AMSU brightness temperatures with those predicted using coincident National Centers for Environmental Prediction (NCEP)-initialized cloud-resolving 5-km resolution fifth-generation National Center for Atmospheric Research/Penn State Mesoscale Model (MM5) [8] 4–6-h forecasts for 106 global storms, and general agreement was found at all opaque wavelengths without empirical corrections. This agreement was achieved using discrete-dipole electromagnetic calculations for icy hydrometeors modeled as hexagonal plates (snow) and six-pointed rosettes (graupel) having observed dimensional ratios, where

Manuscript received September 25, 2008; revised May 19, 2009. Current version published October 28, 2009. This work was supported in part by the National Aeronautics and Space Administration under Grant NNX07AE35G and in part by the Prince of Songkla University under Grant PSU 977/301.

C. Surussavadee is with the Research Laboratory of Electronics, Massachusetts Institute of Technology, Cambridge, MA 02139 USA, and also with the Andaman Environment and Natural Disaster Research Center, Faculty of Technology and Environment, Prince of Songkla University, Phuket Campus, Phuket 83120, Thailand (e-mail: pop@alum.mit.edu).

D. H. Staelin is with the Research Laboratory of Electronics, Massachusetts Institute of Technology, Cambridge, MA 02139 USA (e-mail: staelin@mit.edu).

Digital Object Identifier 10.1109/TGRS.2009.2029093

the MM5-predicted altitude mass distributions of five hydrometeor species were used to infer their exponential size distributions [1], [4]; the Goddard cloud physics model was used [9]. If MM5 overestimates ice and graupel production, then the neural network (NN) would associate MM5 rain with stronger microwave signatures, causing MM5 rain to be underestimated, which does not seem to be the case, as shown later. In fact, the agreement between the predicted and observed AMSU brightness temperature histograms was fairly sensitive to modifications of various MM5 and radiative transfer parameters [10] so no large systematic model errors apparently exist.

The first papers employing absorption to detect precipitation used its spatial [11] or spectral [12], [13] signatures, but these were challenged by diverse surface emission spectra over land that can provide positive, negative, or neutral contrast. Two remedies further increased the observed spectral degrees of freedom: dual polarization [14]–[17] and use of more window frequencies [1]. Although polarization information primarily reduces uncertainties introduced by surface emissivity, it can also help characterize hydrometeors at frequencies where surface effects are negligible.

The retrieval physics employed in this paper is essentially the same as referenced above but without the use of dual polarization. The residual surface effects noted in earlier retrievals using the U.S. National Oceanic and Atmospheric Administration (NOAA) and NASA AMSU [1] have now been reduced to the degree that retrieved snowfall rates over snow and sea ice appear reasonable almost everywhere except for high surface elevations and excessively cold tropospheres. The following sections describe the current AMSU retrieval algorithm and evaluate it against simulations, other satellite data, and rain gauges, leading to identification of challenges to be addressed in future algorithmic iterations.

II. ALGORITHM

This new five-step algorithm improves a similar one demonstrated using AMSU on operational NOAA satellites [1], [18] by relying less on surface channels. To improve AMSU/MM5 retrievals over snowy or icy surfaces, Step 1 omits pixels for which: 1) any brightness temperature is less than 50 K or greater than 400 K (i.e., “invalid”); 2) the atmosphere is so cold and potentially dry that even 183 ± 1 GHz may sense the surface and yield false detections of precipitation, where this potential situation is assumed when AMSU-A channel 5 (53.6 GHz) senses less than 242 K (an empirical threshold based on AMSU data); or 3) the surface altitude is above 2 km for $|\theta_{\text{lat}}| < 60^\circ$, or above 1.5 km for $60 \leq |\theta_{\text{lat}}| < 70^\circ$, or above 0.5 km elsewhere; high-altitude surfaces can be snow covered and are sensed more strongly. When A5 registered below 242 K, the retrieval was set to zero and included in cumulative statistics because precipitation is minimal in such situations and too many pixels experience such cold sometime during any year; therefore, cold-region annual retrievals represent a fairly tight lower bound to corrected values.

Step 2 is shown in Fig. 1. For all scan angles, it estimates: 1) the equivalent brightness temperatures at nadir using separate NNs for land and sea for each AMSU channel and

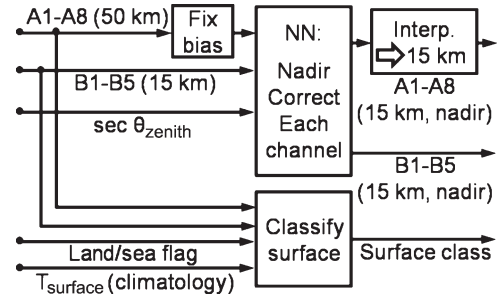


Fig. 1. Step 2 of the AMSU/MM5 algorithm.

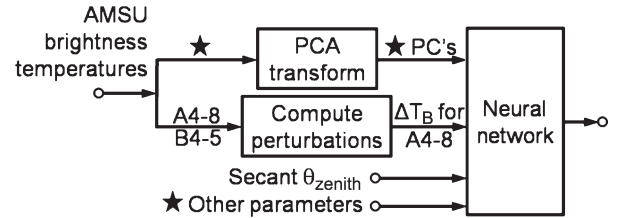


Fig. 2. Architecture of Step 3 of the precipitation retrieval algorithm; * indicates parameters listed in Table I.

2) the surface classification. In the figure, A1–A8 indicate the brightness temperatures (T_B) for AMSU-A channels near 23.8, 31.4, 50.3, 52.8, 53.6, 54.4, 54.9, and 55.5 GHz, respectively; and B1–B5 indicate AMSU-B channels at 89 , 150 , 183 ± 1 , 183 ± 3 , and 183 ± 7 GHz, respectively. To estimate AMSU-A brightness temperatures at nadir, the NN inputs were the secant of the satellite zenith angle and MM5-simulated brightness temperatures for A1–A8. To estimate AMSU-B brightness temperatures at nadir, the NN inputs were MM5-simulated brightness temperatures for AMSU-B channels 1–5 and the secant of the satellite zenith angle. In both cases, the target was the MM5-simulated brightness temperature at nadir for the same pixel. The estimated AMSU-A brightness temperatures at nadir were then bilinearly interpolated to AMSU-B footprints. The MM5 data set is sufficiently large and diverse that tuning each channel to nadir separately introduced no appreciable small-sample noise.

Artificial NNs efficiently compute factored polynomial approximations to the desired multivariate relation between the NN inputs and the output retrieval [19]. The NN polynomial coefficients are determined by iteratively revising their random initial values using “back propagation” to minimize retrieval errors for a “training set” consisting of many pairs of vectors (often $> 10^5$), each representing a plausible input and its desired corresponding output. Our NN outputs were all scalar quantities, not vectors; this required many NNs [1], [18]. The NNs were trained using 106 globally and seasonally distributed MM5 simulations of storms. They were a random subset of 122 storms for which the MM5 forecast brightness temperatures were more consistent with concurrent AMSU observations than were 133 other storms observed over one year; the NCEP 1° initialization was often problematic for the rejected storms [1], [4]. The reduction to 106 storms was forced by limited disk space.

Step 3 produces precipitation-rate retrievals via a path that depends on whether the pixel is land or ocean, its latitude,

TABLE I
INPUTS AND TRAINING FOR STEP 3 OF THE PRECIPITATION RATE ALGORITHM

	Case	Inputs to PCA transform	PCA training	Other inputs to neural net	Neural net training
A	Land	A4-8	Land; 122 orbits	PC1, B3-4	106 MM5, land
B	Sea $ \text{lat} < 45^\circ$, and $53.6 \text{ GHz} > 248 \text{ K}$	A1-8, B1-5	Ice-free sea, 122 AMSU orbits	PC2-5	106 MM5, ice-free sea
C	All sea pixels that are not B	A4-8	Sea $53.6 < 248 \text{ K}$, 122 orbits	PC1-2, B3-4	106 MM5, $53.6 < 248 \text{ K}$, sea
D	All sea	A4-8	Same as C	Same as C	106 MM5, sea

and its brightness temperature at 53.6 GHz. The architecture of Step 3 is shown in Fig. 2. The inputs to the boxes in Fig. 2 and any associated training data sets are further defined for four cases in Table I. Step 3: 1) generates land and sea principal component (PC) scores for PCs observed to be globally sensitive to precipitation but insensitive to most surface effects even though these PCs were computed for channels that sense the surface; 2) computes local brightness temperature perturbations ΔT_B in ~ 54 -GHz channels due to precipitation in zones where 183-GHz radiances below certain thresholds suggest there is precipitation topped by snow or graupel; and 3) combines the PCs and ΔT_B s with the secant of the satellite zenith angle and any other parameters, and presents them to the appropriate NN.

Over land (Algorithm A), the improvements relative to the previous algorithm [1] were to exclude all AMSU-B channels from computation of PCs and to exclude all surface-sensitive oxygen-band channels below 52 GHz. These changes reduced the number of strong degrees of freedom in land brightness temperature spectra that were adding noise to the precipitation retrievals. As a result of this improvement in signal-to-noise ratio the precipitation-sensitive PC was promoted from the second PC (PC2) to the first PC (PC1) because its eigenvalue became the largest.

The final precipitation-rate retrieval P for all ocean pixels, including sea ice, is computed in Step 4:

$$P \text{ (mm/h)} = [kB + (1 - k)C + D] / 2 \quad (1)$$

where $k = 0$ for $|\text{lat}| > 50^\circ$, $k = 1$ for $|\text{lat}| < 40^\circ$, $k = (50 - |\text{lat}|)/10$ for $40^\circ < |\text{lat}| < 50^\circ$, and B , C , and D are the intermediate retrieved precipitation rates using algorithms B, C, and D, respectively, as defined in Table I and Fig. 1. The parameter k varies between 40° and 50° latitude to provide a smooth transition between the empirically identified equatorial and polar regions. This partly location-dependent weighted average of multiple NN estimates for each retrieved pixel is the main innovation in this retrieval architecture beyond its new parameter values. Combining NN outputs trained for different physical circumstances was empirically found to improve detection and reduce false alarms.

Over ocean, the improvements to the previous algorithm [1] are more complex because path B of Table I was replaced by the three paths B, C, and D that are combined by (1). Path B is the ocean algorithm used in [1], which works well for warm ocean but otherwise yields some false detections; therefore, path B is now used only over warm ocean. To avoid false detections over cold ocean, only the more opaque channels were used in paths C and D, where C was trained specifically for cold ocean and D was trained globally. Paths B and C are combined to

yield a global estimator that transitions linearly with latitude between warm (B) and cold (C) over the 40° – 50° latitude band. D itself is also a global estimator for ocean. Results from paths B and C are averaged with those from path D. This averaging of NN outputs was motivated by the discovery during testing that they detected slightly different precipitation events, all of which tended to be consistent with roughly coincident CloudSat observations of precipitation.

It was also discovered that rare cases of extremely dry air over snow or ice surfaces could produce false detections of rates that usually exceeded 3 mm/h, perhaps by an order of magnitude. Much of the problem is due to the unpredictable and possibly low emissivity values of snow and ice and the fact that, even using NWP analyses, these extremely dry cases are currently undetectable with any reliability except when they yield nonphysical precipitation rates. Step 5 deletes all such high rates over snow and ice, even at the expense of deleting a few legitimate retrievals at the high-rate cores of large systems; any precipitation at pixels within ~ 30 km of such deleted pixels is also deleted. The 3-mm/h threshold represents an empirical compromise between too many false alarms and too many deleted legitimate retrievals. Such deletions are too rare to significantly affect accumulation statistics. Snow and ice surfaces are identified using the AMSU surface classification algorithm [20], which is a modified version of [21]. Future instruments with still more opaque water-vapor channels, perhaps near the 320- or 380-GHz resonances, should help detect such superdry air masses and avoid these deletions of possibly valid retrievals. Infrared spectra do not reliably identify such dry regions because some are cloudy.

III. SIMULATIONS OF RETRIEVAL ACCURACIES

One of the most accurate ways to estimate retrieval accuracies is by evaluating simulated retrievals for a competent cloud-resolving numerical weather prediction (NWP) model such as MM5. It has been shown that such predicted retrieval accuracies are relatively insensitive to the exact physics employed in the simulated NWP model and to the radiative transfer expressions used to convert model parameters to brightness temperatures, provided that the correct physics is known once the satellite is in orbit [10], [20]. This insensitivity arises because the predicted precipitation retrieval accuracies are limited primarily by the broad character of the weighting functions, their limited number, and the variance of surface and hydrometeor parameters, not by the finer details of the physics, although the physics must ultimately be known in order to achieve those accuracies. The physics can be improved and ultimately validated by ground truth, laboratory measurements, and accurate simulations.

TABLE II

RMS AND MEAN ERRORS (MM5—ESTIMATE) FOR 15-km RESOLUTION MM5-SIMULATED SURFACE PRECIPITATION RATE RETRIEVALS (IN MILLIMETERS PER HOUR, ALL LATITUDES); RR RANGE IS DEFINED BY MM5

MM5 (mm/h)	RMS Error		Mean Error		RMS Error	
	Land	Sea	Land	Sea	Strat.	Conv.
0.5-1	<i>1.19</i>	<i>1.18</i>	-0.21	-0.46	0.95	<i>3.29</i>
1-2	1.82	1.54	-0.17	-0.33	1.26	<i>4.00</i>
2-4	2.67	2.26	0.17	0.08	1.89	<i>4.12</i>
4-8	4.17	4.35	1.39	0.40	3.62	4.91
8-16	7.70	7.52	3.69	2.69	6.69	7.73
16-32	13.5	13.9	10.0	9.86	-	13.7
32-64	24.6	26.1	20.3	21.8	-	25.5
64	45.8	47.1	41.2	43.8	-	47.2

Italics highlights rms errors that exceed the upper bound listed in column 1 and therefore indicate poor utility. Boldface: rms errors below the minimum listed in column 1, indicating good utility.

TABLE III

RMS AND MEAN ERRORS (MM5—ESTIMATE) FOR 15-km RESOLUTION MM5-SIMULATED SURFACE PRECIPITATION RATE RETRIEVALS (IN MILLIMETERS PER HOUR, ALL LATITUDES); RR RANGE IS DEFINED BY ESTIMATE

AMSU (mm/h)	RMS Error		Mean Error		RMS Error	
	Land	Sea	Land	Sea	Strat.	Conv.
0.5-1	<i>2.09</i>	<i>0.99</i>	0.41	-0.04	0.86	<i>5.24</i>
1-2	2.62	1.69	0.29	-0.04	1.21	<i>6.25</i>
2-4	3.53	3.18	0.24	-0.30	1.78	<i>6.70</i>
4-8	5.98	6.20	0.08	-0.00	2.97	<i>8.08</i>
8-16	9.44	12.01	0.12	0.57	7.01	11.17
16-32	14.0	16.5	1.51	-1.17	15.9	15.4
32-64	28.2	22.9	-1.93	3.74	-	24.9

Italics highlights rms errors that exceed the upper bound listed in column 1 and therefore indicate poor utility. Boldface: rms errors below the minimum listed in column 1, indicating good utility.

TABLE IV

RMS AND MEAN ERRORS (MM5—ESTIMATE) FOR 15-km RESOLUTION MM5-SIMULATED SURFACE PRECIPITATION RATE RETRIEVALS (IN MILLIMETERS PER HOUR) FOR $|LAT| > 45^\circ$; RR RANGE IS DEFINED BY MM5

MM5 (mm/h)	RMS Error		Mean Error		RMS Error	
	Land	Sea	Land	Sea	Strat.	Conv.
0.5-1	0.88	<i>1.03</i>	-0.06	-0.42	<i>0.91</i>	<i>2.40</i>
1-2	1.29	1.39	0.09	-0.21	1.26	2.78
2-4	2.01	2.11	0.60	0.42	1.99	2.70
4-8	3.50	4.98	2.09	0.88	4.31	4.04
8-16	6.61	7.68	5.07	3.64	7.93	6.66
16-32	13.9	-	12.4	-	-	13.9
32-64	24.9	-	23.9	-	-	24.9

Italics highlights rms errors that exceed the upper bound listed in column 1 and therefore indicate poor utility. Boldface: rms errors below the minimum listed in column 1, indicating good utility.

Tables II and III present the rms and mean errors evaluated for the same 106 global storms at 15-km pixels not used for training, while Tables IV and V present similar results for only those pixels at latitudes higher than $\pm 45^\circ$. Approximately 53% of all precipitating pixels in the 106 storms are located at such high latitudes. Tables II and IV stratify the results by the “true” MM5 surface precipitation rate averaged over 15 min. The mean errors (MM5—AMSU) in Tables II and IV dominate the rms errors at high precipitation rates because the highest MM5 precipitation rates are spatially small and are often offset slightly in time and space from the peaks of the AMSU-sensed hydrometeor populations. The rms and mean

TABLE V

RMS AND MEAN ERRORS (MM5—ESTIMATE) FOR 15-km RESOLUTION MM5-SIMULATED SURFACE PRECIPITATION RATE RETRIEVALS (IN MILLIMETERS PER HOUR) FOR $|LAT| > 45^\circ$; RR RANGE IS DEFINED BY ESTIMATE

AMSU (mm/h)	RMS Error		Mean Error		RMS Error	
	Land	Sea	Land	Sea	Strat.	Conv.
0.5-1	<i>1.37</i>	0.79	0.25	-0.01	0.83	<i>3.69</i>
1-2	1.62	1.15	0.11	-0.15	1.13	<i>3.61</i>
2-4	2.73	1.92	0.18	-0.95	1.78	<i>4.70</i>
4-8	4.87	3.66	-0.41	-2.54	3.40	5.51
8-16	8.18	8.21	-0.59	-6.74	8.17	8.20
16-32	9.95	15.9	2.49	-13.8	16.0	12.2

Italics highlights rms errors that exceed the upper bound listed in column 1 and therefore indicate poor utility. Boldface: rms errors below the minimum listed in column 1, indicating good utility.

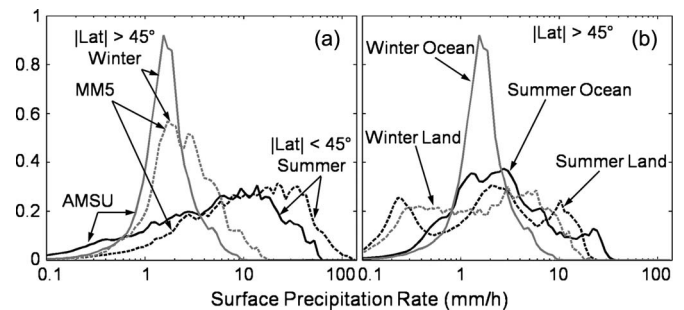


Fig. 3. Normalized equal-area distributions of surface precipitation rate. (a) Solid lines: (gray) AMSU high-latitude winter and (black) low-latitude oceanic summer retrievals for 106 storms over a year; dashed lines: corresponding oceanic MM5 distributions for 106 storms. (b) AMSU retrievals for 106 storms over a year at latitudes higher than $\pm 45^\circ$ for (solid lines) ocean and (dashed lines) land, and for (black lines) summer and (gray lines) winter.

errors for stratiform precipitation are much smaller because the effects of space and time offsets are less due to the greater stability and extent of such storms.

Tables III and V use the AMSU-estimated rain rate to stratify the same results, which were computed using the same NN. The mean errors are now much closer to zero because the NN is trained to minimize errors in each AMSU category, and that AMSU-defined category is known to the network. Mean errors are larger for MM5 stratification because the network does not know the MM5 truth. The tabulations include all 15-km pixels for which the MM5 values of either rainwater or snow at 1000 mbar were nonzero. When computing brightness temperatures, all MM5 surfaces were assumed to be free of snow and ice because MM5 provides no such surface information (http://www.mmm.ucar.edu/mm5/documents/MM5_tut_Web_notes/MM5/mm5.htm) and the spectral characteristics of snow and ice vary greatly and somewhat independently of the atmosphere. Instead, the surface signatures were mitigated by using surface-insensitive PCs and frequencies where the atmosphere is opaque.

In the tables, a plainface font indicates rms errors that are within the given octave range and therefore nominally useful, while boldface indicates rms errors less than the lower bound and therefore good. Italics indicate results that are marginal because they exceed the upper bound of the range. Based on these criteria, stratiform retrievals appear generally useful in the 0.5–1 mm/h and higher ranges. Although convective

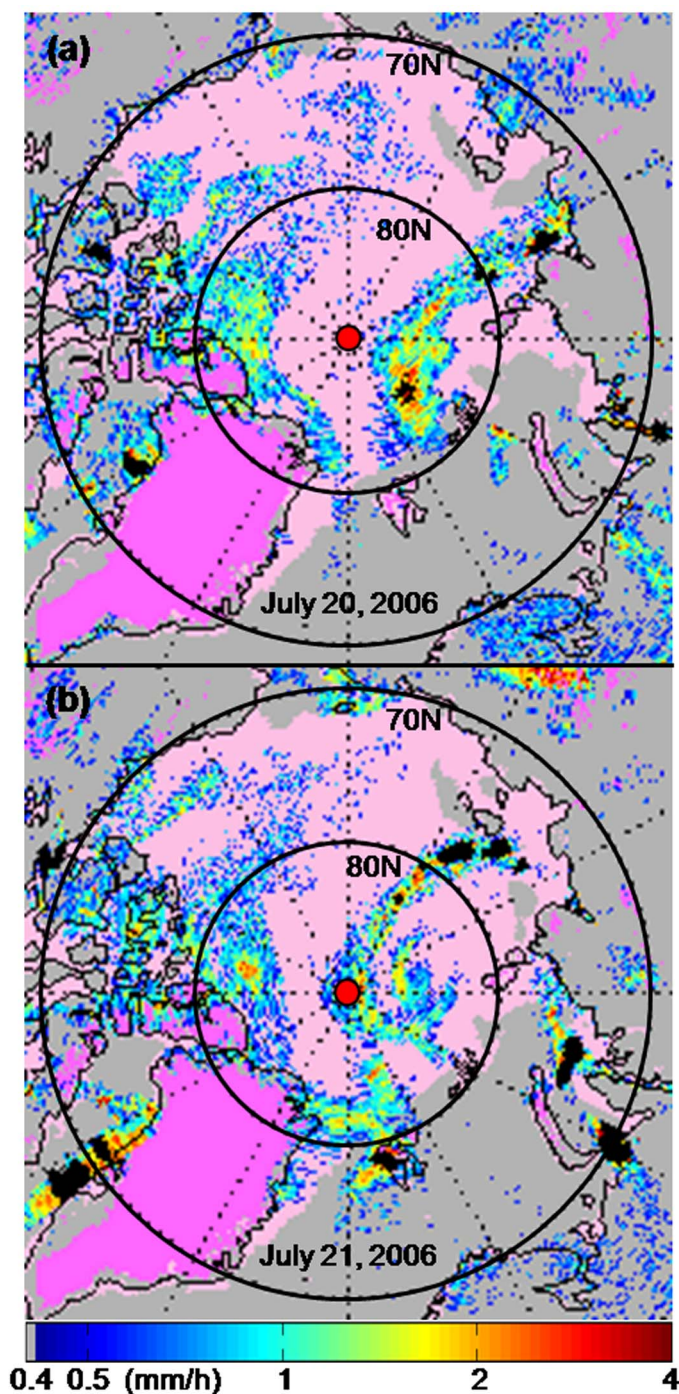


Fig. 4. AMSU-retrieved North Pole precipitation rates over sea ice. (a) July 20, 2006. (b) July 21, 2006. Light pink is snow or sea ice, dark pink is high-elevation land, and black represents rejected retrievals over 3 mm/h for snow/ice surfaces.

precipitation is reliably detected, the rms errors are significantly larger because they are dominated by small spatial and time offsets between the instantaneous hydrometeor populations at the ground and in the sensed cell tops nearby. Convective precipitation retrievals above ~ 4 mm/h are more accurate, as are averages of retrievals, as shown later in Fig. 9. Precipitation was classified as convective using a NN trained with 106 MM5 cases for which convection was defined when the MM5 peak single-layer vertical velocity exceeded 0.45 m/s at 15-km horizontal

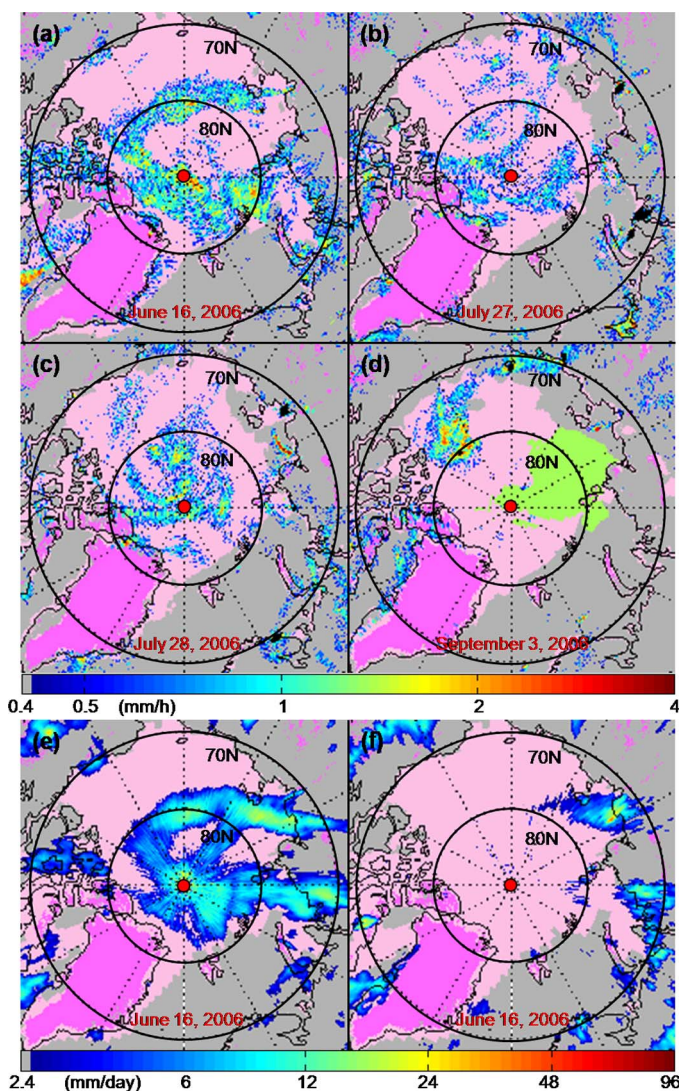


Fig. 5. AMSU-retrieved Arctic precipitation rates over (light pink) sea ice during 2006; the precipitation rate is given by the color code of Fig. 4 for: (a) June 16, (b) July 27, (c) July 28, and (d) September 3. (e) and (f) are daily average precipitation (in millimeters per day) for AMSU and GPCP, respectively, for June 16. Light pink is snow or sea ice, green indicates tropopause air temperatures that are too low to permit reliable retrievals, dark pink is high-elevation land, and black represents rejected retrievals over 3 mm/h for snow/ice surfaces.

resolution. This velocity threshold was chosen to balance and minimize misclassifications of both types of precipitation [4].

Over ocean, the indicated accuracies for rain and snowfall were approximately the same. The nominal rain/snow distinction was based upon tropospheric temperatures, i.e., whether the brightness temperature at 53.6 GHz was above or below 248 K, a tropospheric temperature threshold selected by balancing the total probabilities of false and missed detections computed using MM5 simulations. This equality of performance was expected because AMSU precipitation signatures arise more from cell-top hydrometeors than from the rate or phase of those impacting the surface.

Fig. 3 shows the retrieved and MM5 surface precipitation rate distributions for various categories of pixels over the same 106 global storms presented in Tables II–V, which span a year from July 1, 2002 to June 30, 2003 [4]. Fig. 3(a) shows the

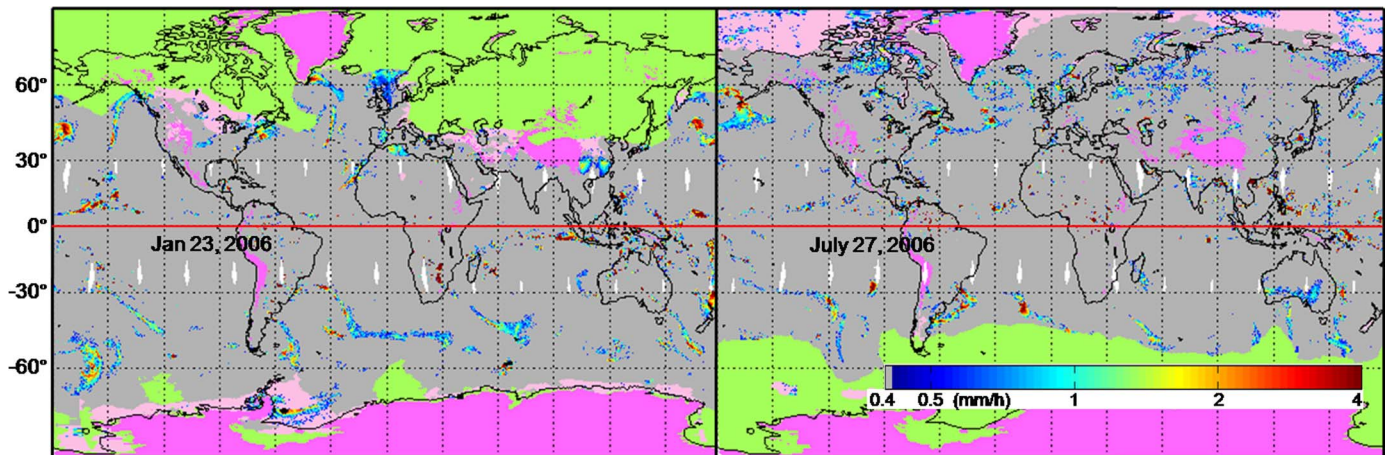


Fig. 6. Typical (left) winter and (right) summer 24-h images showing seasonal extremes. Light pink is snow or sea ice. Green indicates tropopause air temperatures that are too low to permit reliable retrievals. Dark pink is high-elevation land, and black represents rejected retrievals over 3 mm/h for snow/ice surfaces.

area-normalized annual AMSU and MM5 oceanic precipitation distributions for winter at latitudes higher than $\pm 45^\circ$, and for summer below $\pm 45^\circ$. The winter distributions peak near 2 mm/h while the more convective summer precipitation peaks above 10 mm/h. AMSU is probably biased toward lower rates than MM5 because mean-square estimators always tend to bias estimates toward the true mean (defined by MM5), which is lower.

Fig. 3(b) shows the AMSU-retrieved distributions at latitudes higher than $\pm 45^\circ$ for the four land/sea, summer/winter cases, where summer was defined as the three months, namely, June, July, and August, for the Northern Hemisphere, plus the opposite months in the southern hemisphere; winter includes the opposite three-month sets. In all cases, little surface rain was detected at rates below 0.1 mm/h or above 10–30 mm/h, the higher bounds being established largely by the spatial resolution of AMSU (≥ 15 km) and the responsiveness of AMSU to convective cells with overspread icy cell tops rather than to surface precipitation rates. The nonuniformity of these distributions is probably real and variable year to year since a few large storms can dominate annual statistics.

IV. RETRIEVAL RESULTS: IMAGES AND AVERAGES

The most obvious improvement is the new algorithm's ability to retrieve meteorologically plausible precipitation patterns and rates over the Arctic ice cap, as shown in Figs. 4 and 5. Fig. 4 shows that the Arctic is meteorologically quite active in July, and Fig. 5 shows that such activity extends over the full summer and that arctic fronts have a strong tendency to swirl due to Coriolis forces. Geographic coverage is principally limited by the high elevation of Greenland and the excessively cold air that dominates from about October 1 to April 20; these exclusions are necessary because both altitude and excessive cold currently increase the probability of false detections due to surface effects. Despite these coverage limits, routine Arctic precipitation can now be obtained for about five months per year several times daily with 15-km resolution back to 1999, starting with NOAA-15. This new capability should greatly

enhance our ability to understand the effects of precipitation on the rapidly evolving arctic climate. For example, the effects of precipitation on the evolution of sea ice, tundra, and methane production will become more evident, as will the influence of sea ice and tundra on precipitation. The novelty of this new capability to monitor Arctic precipitation north of 80° N is shown by the comparison in Fig. 5(e) and (f) between the AMSU and Global Precipitation Climatology Project (GPCP) [22] 24-h rates estimated for June 16, 2006.

Fig. 6 shows equatorial views of the Earth for January 23 and July 27, 2006 that again suggest how surface elevation (dark pink) and excessive cold (green) limit the geographic range of useful retrievals near the peak summer and winter days. Each pixel has the value most recently observed at that location during that 24-h period. The ascending equatorial local crossing time for NOAA-16 was then ~ 4 P.M. Because storms move between orbits, parts of some storms may be viewed twice. The unobserved portions of the Earth (white) are small and should essentially vanish for the future wide-swath Advanced Temperature and Moisture Sounder scheduled to replace AMSU on future satellites [23], [24]. The images show that strong convective storms (red) often occupy no more than a few pixels, and that most precipitation occurs in frontal systems with a significant stratiform component. The July 27 image also exhibits a remarkably large fully developed spiral system just south of Greenland.

Fig. 7 shows the inferred annual total precipitation (in millimeters per year) and the probability of retrieving 15-km-resolution precipitation above 0.5 mm/h, as observed in 2007 by NOAA-16 when the ascending node was ~ 4 P.M. The threshold for precipitation detection was 0.5 mm/h at ~ 15 -km resolution. Each pixel represents a single box measuring 0.15° on a side. The main equatorial features include the split intertropical convergence zone (ITCZ) and the dry eastern portions of the Atlantic and Pacific oceans; the main polar features include the wet arctic and the increased contrast between land and sea along certain coastlines. Whether the origin of these coastal precipitation gradients is meteorological or an observation artifact requires further study. For example, Canada, Alaska, and Northern Europe exhibit less precipitation than their immediately

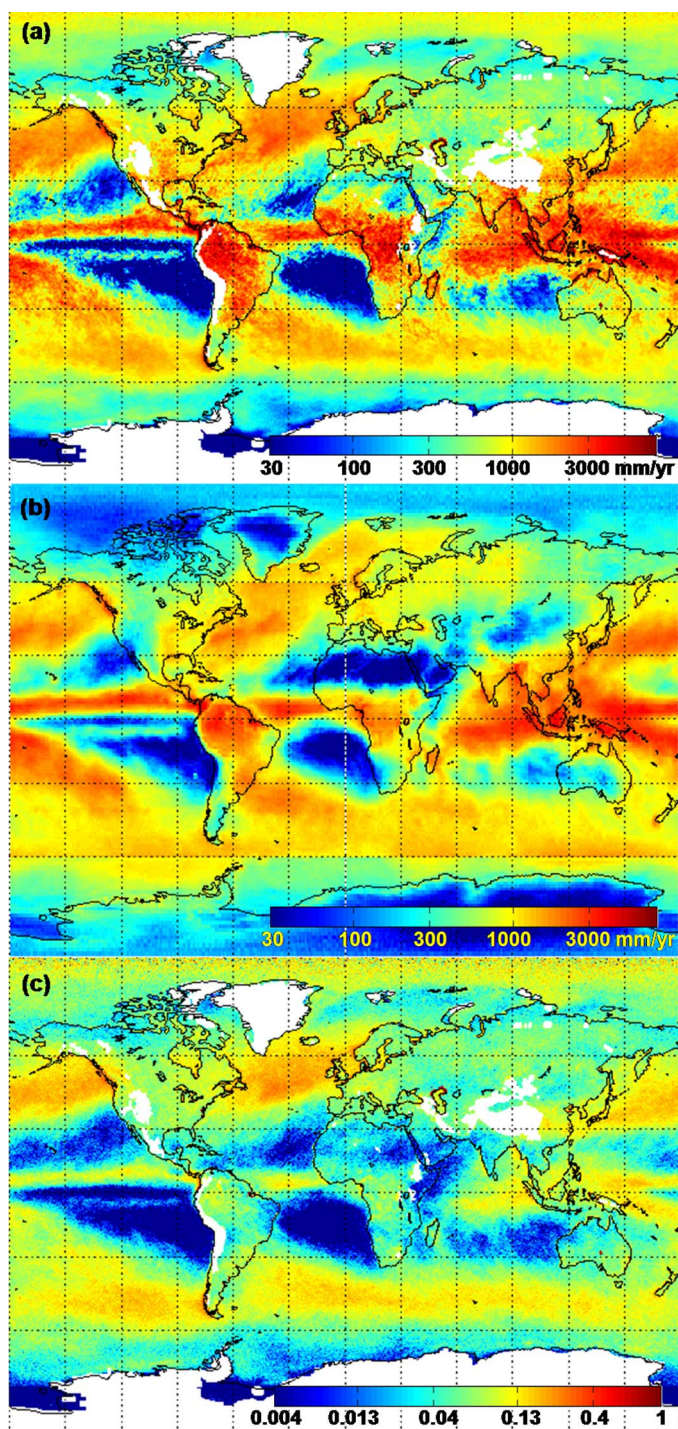


Fig. 7. Global annual averages for 2007 of (a) AMSU precipitation (in millimeters per year) in 0.15° boxes, (b) GPCP precipitation within 1° boxes, and (c) AMSU probability of precipitation over 0.5 mm/h in a ~ 15 -km pixel per overpass.

adjacent ocean, while the ratio is somewhat reversed for Brazil and otherwise nearly zero north of 60° N and around much of Australia and other land masses. For comparison, Fig. 7(b) shows the GPCP annual accumulations in 1° cells for the same year shown in Fig. 7(a) for AMSU. Significant differences include the lower desert and Arctic values estimated by GPCP, higher GPCP values over Europe and western Siberia, and the discontinuity at 60° S.

The AMSU precipitation probability distributions in Fig. 7(c) are quite similar for Siberia, Canada, and the ITCZ over land, and the highest indicated probabilities occur in the North Pacific and North Atlantic oceans. Such features will be among the first analyzed as this algorithm is refined further.

Fig. 8 shows for 2007 the latitudinal annual accumulations for precipitation (in millimeters per year) and the probability of instantaneous 15-km precipitation rates above 0.5 mm/h. These averages have been divided into rain versus snow on the basis of air temperature, and into convective versus stratiform precipitation on the basis of estimated vertical wind velocities. The highest observed average latitudinal precipitation probability and amount are 13% and 2470 mm/yr, respectively. The importance of accurately estimating stratiform precipitation is indicated by the result that outside the tropics stratiform precipitation is more than an order of magnitude more common than convective precipitation and contributes more total precipitation. The increase in both snow and rain north of 80° N is interesting and appears to be real. These annualized results at tropical latitudes are comparable to those reported by others [25].

V. COMPARISONS WITH ANNUAL RAIN GAUGE DATA

Rain gauges are often used as the “gold standard” for precipitation measurements. Fig. 9 shows the comparison of: 1) annualized averages of all AMSU retrievals (in millimeters per hour) within $\pm 0.4^\circ$ longitude and latitude of each rain gauge, where the averages include zeros, to 2) the annual accumulations (in millimeters) reported by NOAA at 345 rain gauge sites [26]. These sites were observed by NOAA-16 for 2007 within $\pm 0.4^\circ$ longitude and latitude. The 345 sites do not include 195 sites that were omitted because their surface elevation varied more than 500 m within an area bounded by $\pm 0.2^\circ$ from the site; such hilly sites are subject to unknown orographic effects; because of overlapping, fewer than 345 points are visible. This empirical terrain criterion eliminated most outliers but little else. In addition, another 39 desert sites with annual surface rain gauge accumulations below 300 mm were omitted because they appeared to be significantly overestimated by AMSU due to near-surface evaporation not distinguished from rainfall; for these sites AMSU typically estimates rates near 300 mm/yr.

Locations near coastlines, particularly convoluted ones, can also introduce uncertainties, so Fig. 9 separately indicates with \times s all 114 sites within 55 km of the coast. If the problematic coastal sites are omitted, then 231 nondesert sites remain that are located away from mountains and are therefore more trustworthy. The AMSU estimates in Fig. 9 typically exceed rain gauge measurements near coasts. This bias is almost entirely positive and consistent with the ocean/land discontinuities evident in Fig. 7(a) along most coastlines. These coastal gradients are probably due to some combination of antenna sidelobe effects, systematic local meteorological phenomena, and small pixel location errors. In addition, false AMSU precipitation detections due to surface effects are occasionally evident too, so the next iteration of this algorithm must address all three issues.

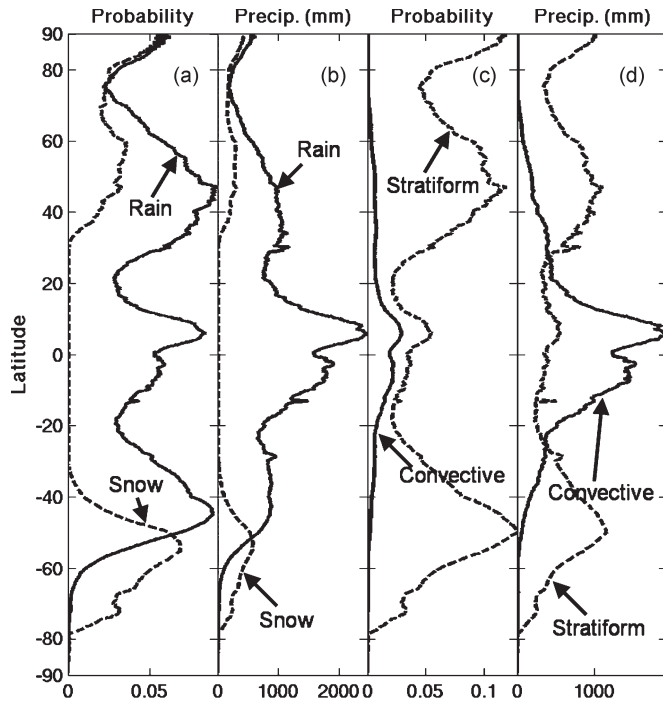


Fig. 8. Latitudinal dependences in 2007 for rain and snow: (a) probability distributions and (b) cumulative distributions (in millimeters). Dependences for stratiform and convective precipitation: (c) probability distributions and (d) cumulative distributions (in millimeters). All detections exceed 0.5 mm/h with ~ 15 -km resolution.

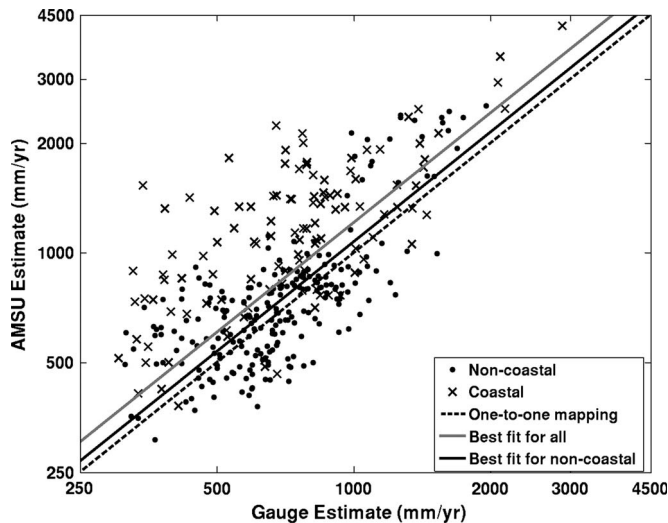


Fig. 9. Comparison of AMSU and rain gauge annual precipitation (in millimeters) for 2007 at 345 globally distributed nondesert sites in nonmountainous regions. Sites within 55 km of coastline are indicated by \times . (Dashed line) One-to-one mapping. (Black line) Logarithmic least squares best fit for a single scale factor correction for noncoastal sites. (Gray line) Similar best fit for all sites.

The logarithmic least squares best fit to a constant correction factor for all sites, shown by the gray line in Fig. 9, suggests that the AMSU retrieval is biased high relative to the dashed zero-bias line by 198 mm/yr, or 26% of the corresponding average rain gauge data. However, when the problematic coastal sites are omitted (black line), this bias becomes 78 mm/yr, which corresponds to 10.7% of the average rain gauge data.

The rms logarithmic deviation for the noncoastal sites with respect to these best fit lines is $\pm 29\%$, due to a combination of

sampling errors and site-specific biases. Subsequent comparisons of such data for two years suggest that sampling errors are significant when these annual accumulations are dominated by a few large storms, e.g., short-lived convective events that may or may not be observed when Nimbus 16 passes overhead every 12 h [7]. In particular, the ratio of the standard deviation of a Poisson process to its mean is $\sim 1/\sqrt{N}$, assuming N equal-size samples (e.g., rain storms) are summed; 29% corresponds to $N \cong 12$. Such sampling noise is reduced when all significant storms are observed or are frequent and of uniform size. Additional studies are required to segment these error contributions and to reveal if and why AMSU consistently tends to overestimate accumulation rates for sites reporting more than 1000 mm/yr, as shown by the figure.

This generally good agreement with rain gauge data over a large dynamic range (~ 300 – 3000 mm/yr) was achieved without algorithmic tuning, i.e., the only physics employed by the algorithm resides in: 1) MM5 [4], [8]; 2) the Goddard cloud-resolving physics model [9]; 3) the radiative transfer program (TBSCAT) [20] used for training; and 4) the discrete dipole electromagnetic discrete-dipole model (DDSCAT) scattering calculations for snow (hexagonal plates), graupel (six-pointed rosettes), and other hydrometeor species [4]. No empirical adjustments were used to close the gap between the algorithm and rain gauge or other ground truth data. A subsequent paper [7] provides surface-classification-dependent corrections to these precipitation estimates based on more extensive AMSU observations and gauge comparisons; the largest corrections are required over daytime desert and grassland sites which appear often to exhibit virga.

VI. COMPARISONS WITH CLOUDSAT

Nearly simultaneous radar is the most reliable tool for determining whether AMSU precipitation detections are real or due to surface effects or dense clouds. Fortunately, the nadir-looking CloudSat radar typically observes the same events within a few minutes to a few hours [27], [28]. Fig. 10 shows seven representative comparisons at high latitudes: one over the Antarctic ice shelf, one over Canadian snow, one over the North Atlantic involving both snowfall and rain (rain is indicated by the bright band in the radar image), a front over Labrador, and three snowstorms over the Arctic ice cap. These significant events beyond $\pm 50^\circ$ latitude are typically long lived, mostly stratiform, and can be tracked over multiple satellite passes, so these 24–180-min gaps between AMSU and CloudSat observations are not unreasonable (as they would be for short-lived convective events). For example, note the similarity between Fig. 5(a) (instantaneous) and Fig. 5(e) (24-h average).

The possible false detection on May 15 could be due to virga or to weather changes prior to CloudSat's passage 80 min later. The data for December 15 suggest that AMSU can perhaps distinguish, from the hydrometeors above, precipitation at altitudes as low as ~ 2 – 3 km, but cannot distinguish the narrow precipitation column impacting the surface at any instant. This follows from the fact that the width of the AMSU-sensed precipitation band is wider than the radar-indicated band of hydrometeors reaching Earth at that instant, but narrower than

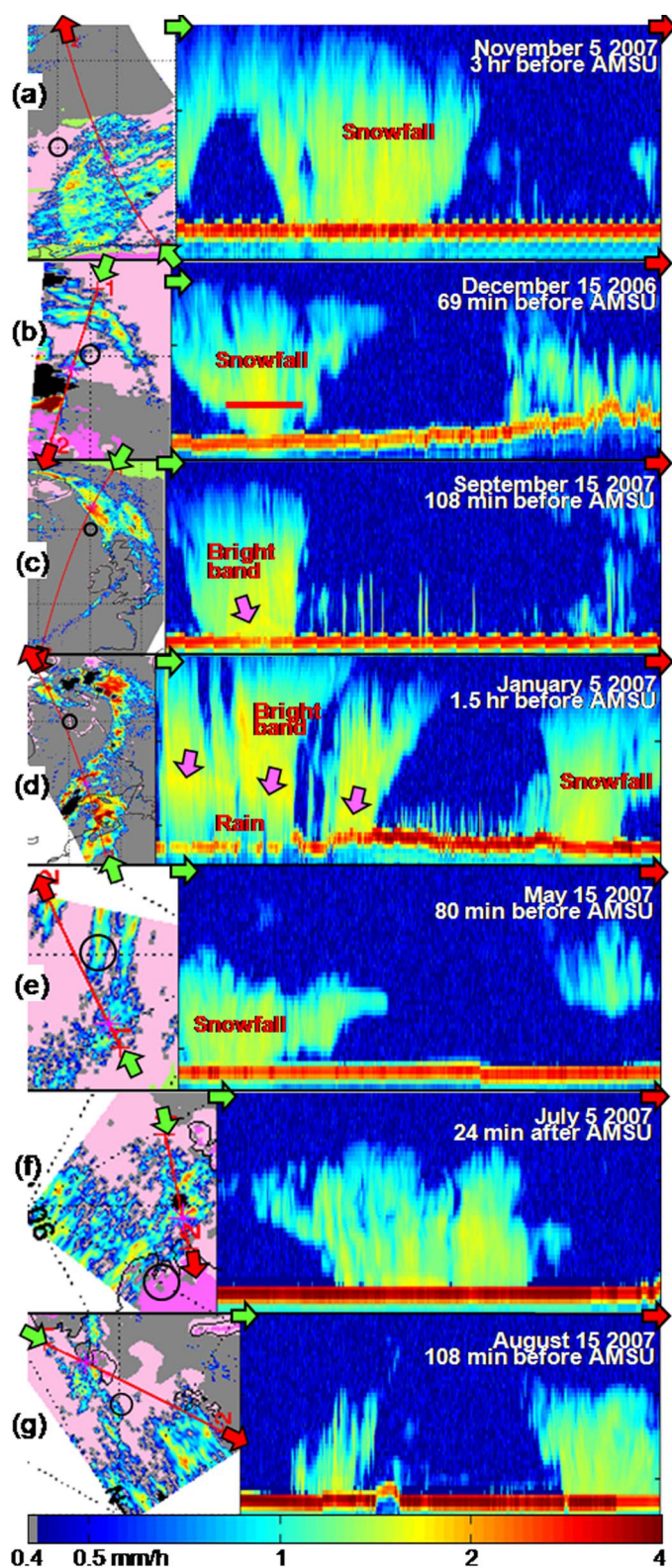


Fig. 10. Comparisons of AMSU surface-precipitation retrievals and CloudSat echo strengths. The CloudSat orbit is red and bounded by red and green arrows; its peak illustrated echo altitude is ~ 12 km. Pink, dark pink, and black pixels indicate surface snow or ice, excessive surface elevation, and untrustworthy retrievals, respectively. Gray is land or water. The 200-km-diameter black circles are centered at (a) 60° S/ 20° E over Antarctic ice shelf, (b) 50° N/ 110° W over Canadian snow, (c) 60° N/ 10° W near a North Atlantic front, (d) 60° N/ 70° W over Labrador coastline, and over Arctic ice pack at (e) 82° N/ 180° E, (f) 82° N/ 30° W, and (g) 82° N/ 90° E.

the band of hydrometeors above 4-km altitude. The algorithm's cloud penetration depth is determined by scattering and absorption near 53 GHz. AMSU frequencies are generally insensitive to hydrometeors too small to fall at significant velocities. Again, the 69-min offset introduces some uncertainty.

Review of other CloudSat data suggests that although AMSU is less sensitive to events lacking hydrometeors above ~ 2 km, such low-altitude precipitation seldom dominates statistics except in special cases like lake-effect snowfall. Over ocean, the total opacity of hydrometeors is sensed, so that the altitudes of storms having high millimeter-wave opacity are not important. Over land, cold low-altitude hydrometeors usually have ice-scattering signatures that vary informatively across 183-GHz channels having different water-vapor opacities, and most low-altitude warm precipitation can be detected near 183 GHz because unglaciated hydrometeors above ~ 2 km stand out if the lapse rate is adequate.

VII. SUMMARY AND CONCLUSION

The two principal advances were that: 1) AMSU can now retrieve rain and snowfall rates over snow and ice surfaces by channel omissions and PC filtering that reduce the spectral effects of unpredictable surface variations and 2) comparison with a global set of nondesert rain gauges suggests that annual AMSU precipitation measurements by NOAA-16 are biased high by only $\sim 11\%$ before any algorithmic "tuning" to ground truth is employed, provided coastlines, mountains, and deserts are avoided. Some portion of this indicated bias may be due to diurnal observational effects. This lack of significant bias suggests that the physics imbedded in MM5, the two-stream scattering model (TBSCAT), and the modeled scattering behavior of hexagonal plates (snow) and six-pointed rosettes (graupel) are all reasonably faithful to nature, and that this physics has furthermore been reasonably inverted by the nonlinear stochastic approach to precipitation retrieval adopted here.

There is room for further improvement, however. For example, sampling errors probably account for a significant fraction of the scatter in the annual estimates due to use of data from only one satellite, and no use has yet been made of prior information contained in concurrent NWP data or data from other sensors such as infrared imaging spectrometers or microwave scatterometers. Furthermore, the present inability to retrieve snowfall rates below a threshold tropospheric temperature can be largely remedied by incorporating a few additional channels at a more opaque water-vapor resonance such as 380 GHz. Then, even when extremely cold dry descending air renders all 183-GHz channels transparent to the surface, the remaining opaque channels could still sense hydrometeors free from surface noise. Retrievals over high elevations such as the Himalayas would also be improved. Unfortunately, our preliminary efforts to detect cold dry air using opaque infrared channels were frustrated by the occasional appearance of clouds even when the surface was visible near 183 GHz, and efforts to use concurrent NWP data failed because they often significantly underestimate the severity of extremely cold dry descending air columns, perhaps because of NWP gravity-wave filters.

The greatest opportunity for improvement, however, probably lies in methods that can reduce the misleading effects of hydrometeor evaporation near the surface, as evident in our rain gauge comparisons with desert sites that accumulate less than 300 mm/yr. Some correction for virga is already incorporated in the NN used over land because its inputs include the temperature and humidity profile information resident in AMSU-A channels 4–8 and AMSU-B channels 3–4, and in the rain-cell-altitude information imbedded in the ΔT inputs. Since passive microwaves cannot directly detect clear air below virga, the primary remaining approach to wide-swath virga detection is to combine AMSU hydrometeor altitude and intensity information with NWP subcloud temperature, humidity, and wind information; this hypothesis will be tested.

Finally, there are opportunities for refining the architecture of the algorithm and enlarging the training sets that define its physics. For example, the two-stream radiative transfer model could be replaced by a multistream model, and the planar atmosphere assumption could be replaced by 3-D models that include the effects of tall convective cells viewed at large zenith angles. In any event, the global AMSU data presented here provide benchmarks against which such improvements and other sensors can be compared in order to track progress in global precipitation measurement and suggest possible future improvements.

ACKNOWLEDGMENT

The authors would like to thank Pennsylvania State University and the University Corporation for Atmospheric Research for providing the MM5 and technical support; the Alliance for Computational Earth Science, Massachusetts Institute of Technology, for assisting with computer resources; P. W. Rosenkranz for his forward radiance program, TBSCAT, and helpful discussions; L. von Bosau for help with the rain gauge data; and A. Graumann, C. Nichols, and L. Zhao of the NOAA/National Environmental Satellite, Data, and Information Service for help with AMSU data.

REFERENCES

- [1] C. Surussavadee and D. H. Staelin, "Global millimeter-wave precipitation retrievals trained with a cloud-resolving numerical weather prediction model, Part I: Retrieval design," *IEEE Trans. Geosci. Remote Sens.*, vol. 46, no. 1, pp. 99–108, Jan. 2008.
- [2] D. H. Staelin and F. W. Chen, "Precipitation observations near 54 and 183 GHz using the NOAA-15 satellite," *IEEE Trans. Geosci. Remote Sens.*, vol. 38, no. 5, pp. 2322–2332, Sep. 2000.
- [3] F. W. Chen and D. H. Staelin, "AIRS/AMSU/HSB precipitation estimates," *IEEE Trans. Geosci. Remote Sens.*, vol. 41, no. 2, pp. 410–417, Feb. 2003.
- [4] C. Surussavadee and D. H. Staelin, "Comparison of AMSU millimeter-wave satellite observations, MM5/TBSCAT predicted radiances, and electromagnetic models for hydrometeors," *IEEE Trans. Geosci. Remote Sens.*, vol. 44, no. 10, pp. 2667–2678, Oct. 2006.
- [5] D. H. Staelin, A. L. Cassel, K. F. Kunzi, R. L. Pettyjohn, R. K. L. Poon, P. W. Rosenkranz, and J. W. Waters, "Microwave atmospheric temperature sounding: Effects of clouds on the Nimbus 5 satellite data," *J. Atmos. Sci.*, vol. 32, no. 10, pp. 1970–1976, Oct. 1975.
- [6] T. T. Wilheit, A. T. C. Chang, J. L. King, E. B. Rodgers, R. A. Nieman, B. M. Krupp, A. S. Milman, J. S. Stratigos, and H. Siddalingaiah, "Microwave radiometric observations near 19.35, 92, and 183 GHz of precipitation in tropical storm Cora," *J. Appl. Meteorol.*, vol. 21, no. 8, pp. 1137–1145, Aug. 1982.
- [7] C. Surussavadee and D. H. Staelin, "Global precipitation retrievals using the NOAA/AMSU millimeter-wave channels: Comparisons with rain gauges," *J. Appl. Meteorol. Climatol.*, to be published.
- [8] J. Dudhia, D. Gill, K. Manning, W. Wang, and C. Bruyere, PSU/NCAR Mesoscale Modeling System Tutorial Class Notes and Users' Guide (MM5 Modeling System Version 3), Boulder, CO, NCAR, Jan. 2005, [Online]. Available: <http://www.mmm.ucar.edu/mm5/documents/tutorial-v3-notes.html>
- [9] W.-K. Tao and J. Simpson, "Goddard cumulus ensemble model. Part I: Model description," *Terres., Atmos. Ocean. Sci.*, vol. 4, no. 1, pp. 35–72, Mar. 1993.
- [10] C. Surussavadee and D. H. Staelin, "Millimeter-wave precipitation retrievals and observed-versus-simulated radiance distributions: Sensitivity to assumptions," *J. Atmos. Sci.*, vol. 64, no. 11, pp. 3808–3826, Nov. 2007.
- [11] T. T. Wilheit, A. T. C. Chang, M. S. V. Rao, E. B. Rodgers, and J. S. Theon, "A satellite technique for quantitatively mapping rainfall rates over the oceans," *J. Appl. Meteorol.*, vol. 16, no. 5, pp. 551–560, May 1977.
- [12] P. W. Rosenkranz, F. T. Barath, J. C. Blinn, III, E. J. Johnston, W. B. Lenoir, D. H. Staelin, and J. W. Waters, "Microwave radiometric measurements of atmospheric temperature and water from an aircraft," *J. Geophys. Res.*, vol. 77, no. 30, pp. 5833–5844, Oct. 1972.
- [13] D. H. Staelin, A. H. Barrett, J. W. Waters, F. T. Barath, E. J. Johnston, P. W. Rosenkranz, N. E. Gaut, and W. B. Lenoir, "Microwave spectrometer on the Nimbus 5 satellite: Meteorological and geophysical data," *Science*, vol. 182, no. 4119, pp. 1339–1341, Dec. 1973.
- [14] J. A. Weinman and P. J. Guetter, "Determination of rainfall distributions from microwave radiation measured by the Nimbus 6 ESMR," *J. Appl. Meteorol.*, vol. 16, no. 4, pp. 437–442, Apr. 1977.
- [15] P. Gloersen, D. J. Cavalieri, A. T. C. Chang, T. T. Wilheit, W. J. Campbell, O. M. Johannessen, K. B. Katsaros, K. F. Kunzi, D. B. Ross, D. H. Staelin, E. P. L. Windsor, F. T. Barath, P. Gudmandsen, E. Langham, and R. O. Ramseier, "A summary of results from the first Nimbus 7 SMMR observations," *J. Geophys. Res.*, vol. 89, no. D4, pp. 5335–5344, Jun. 1984.
- [16] R. W. Spencer, H. M. Goodman, and R. E. Hood, "Precipitation retrieval over land and ocean with the SSM/I: Identification and characteristics of the scattering signal," *J. Atmos. Ocean. Technol.*, vol. 6, no. 2, pp. 254–273, Apr. 1989.
- [17] C. Kummerow, J. Simpson, O. Thiele, W. Barnes, A. T. C. Chang, E. Stucker, R. F. Adler, A. Hou, R. Kakar, F. Wentz, P. Ashcroft, T. Kozu, Y. Hong, K. Okamoto, T. Iguchi, H. Kuroiwa, E. Im, Z. Haddad, G. Huffman, B. Ferrier, W. S. Olson, E. Zipser, E. A. Smith, T. T. Wilheit, G. North, T. Krishnamurti, and K. Nakamura, "The status of the Tropical Rainfall Measuring Mission (TRMM) after two years in orbit," *J. Appl. Meteorol.*, vol. 39, no. 12, pp. 1965–1982, Dec. 2000.
- [18] C. Surussavadee and D. H. Staelin, "Global millimeter-wave precipitation retrievals trained with a cloud-resolving numerical weather prediction model, Part II: Performance evaluation," *IEEE Trans. Geosci. Remote Sens.*, vol. 46, no. 1, pp. 109–118, Jan. 2008.
- [19] W. J. Blackwell and F. W. Chen, *Neural Networks in Atmospheric Remote Sensing*. Norwood, MA: Artech House, Apr. 2009.
- [20] P. W. Rosenkranz, "Rapid radiative transfer model for AMSU/HSB channels," *IEEE Trans. Geosci. Remote Sens.*, vol. 41, no. 2, pp. 362–368, Feb. 2003.
- [21] N. C. Grody, F. Weng, and R. R. Ferraro, "Application of AMSU for obtaining hydrological parameters," in *Microwave Radiometry and Remote Sensing of the Earth's Surface and Atmosphere*, P. Pampaloni and S. Paloscia, Eds. Zeist, The Netherlands: VSP, 2000, pp. 339–352.
- [22] G. J. Huffman, R. F. Adler, M. M. Morrissey, D. T. Bolvin, S. Curtis, R. Joyce, B. McGavock, and J. Susskind, "Global precipitation at one-degree daily resolution from multisatellite observations," *J. Hydrometeorol.*, vol. 2, no. 1, pp. 36–50, Feb. 2001.
- [23] T. J. Kleespies, "Relative information content of the Advanced Technology Microwave Sounder and the combination of the Advanced Microwave Sounding Unit and the Microwave Humidity Sensor," *IEEE Trans. Geosci. Remote Sens.*, vol. 45, no. 7, pp. 2224–2227, Jul. 2007.
- [24] C. Surussavadee and D. H. Staelin, "NPOESS precipitation retrievals using the ATMS passive microwave spectrometer," in *Proc. IGARSS*, Jul. 2008, pp. V-570–V-573.
- [25] G. J. Huffman, R. F. Adler, P. Arkin, A. Chang, R. Ferraro, A. Gruber, J. Janowiak, A. McNab, B. Rudolf, and U. Schneider, "The Global Precipitation Climatology Project (GPCP) combined precipitation dataset," *Bull. Amer. Meteorol. Soc.*, vol. 78, no. 1, pp. 5–20, Jan. 1997.
- [26] Monthly Climatic Data for the World, Nat. Climatic Data Center (NCDC), Nat. Environ. Satellite, Data, Inform. Service (NESDIS), Nat. Ocean.

Atmos. Admin. (NOAA) Asheville, NC, 2007. [Online]. Available: <http://www7.ncdc.noaa.gov/IPS/mcdw/mcdw.html>

- [27] G. G. Mace, R. Marchand, Q. Zhang, and G. Stephens, "Global hydrometeor occurrence as observed by Cloud Sat: Initial observations from summer 2006," *Geophys. Res. Lett.*, vol. 34, no. 9, pp. L09 808-1–L09 808-5, May 2007.
- [28] 2B-GEOPROF, Dec. 5, 2007. [Online]. Available: <http://www.cloudsat.cira.colostate.edu/>



Chinnawat Surussavadee (S'04–M'07) received the B.Eng. degree in electrical engineering from King Mongkut's Institute of Technology Ladkrabang, Bangkok, Thailand, in 1999, the M.S. degree in electric power engineering from Rensselaer Polytechnic Institute, Troy, NY, in 2001, and the Ph.D. degree in electrical engineering from the Massachusetts Institute of Technology (MIT), Cambridge, in 2007.

From 2004 to 2006, he was a Research Assistant with the Remote Sensing and Estimation Group, Research Laboratory of Electronics (RLE), MIT. From 2006 to 2007, he was a Lecturer with Phuket Rajabhat University, Phuket, Thailand. He is currently a Research Affiliate with RLE and a Lecturer and the Head of the Andaman Environment and Natural Disaster Research Center, Faculty of Technology and Environment, Prince of Songkla University, Phuket Campus, Phuket, Thailand.



David H. Staelin (S'59–M'65–SM'75–F'79–LF'04) received the S.B., S.M., and Sc.D. degrees in electrical engineering from the Massachusetts Institute of Technology (MIT), Cambridge, in 1960, 1961, and 1965, respectively.

He joined the MIT faculty in 1965, where he is currently a Professor of electrical engineering and teaches electromagnetics and signal processing. He was the Principal Investigator for the Nimbus-E Microwave Spectrometer and Scanning Microwave Spectrometer Experiments on the NASA Nimbus-5 and Nimbus-6 satellites and a Coinvestigator of the NASA Atmospheric Infrared Sounder/Advanced Microwave Sounding Unit/Humidity Sounder for Brazil on Aqua, Scanning Multichannel Microwave Radiometer on Nimbus 7, and Planetary Radio Astronomy on Voyagers 1 and 2. From 1990 to 2001, he was an Assistant Director with the MIT Lincoln Laboratory, Lexington, MA.

Dr. Staelin is a member of the U.S. National Polar-orbiting Operational Environmental Satellite System (NPOESS) Sounder Operational Algorithm Team and the NASA science teams for the Precipitation Measurement Missions and the NPOESS Preparatory Program.